



Article

Nonenzymatic Hydrogen Peroxide Detection Using Surface-Enhanced Raman Scattering of Gold–Silver Core–Shell-Assembled Silica Nanostructures

Xuan-Hung Pham , Bomi Seong, Sungje Bock, Eunil Hahm, Kim-Hung Huynh, Yoon-Hee Kim, Wooyeon Kim, Jaehi Kim, Dong-Eun Kim and Bong-Hyun Jun *

Department of Bioscience and Biotechnology, Konkuk University, Seoul 05029, Korea; phamricky@gmail.com (X.-H.P.); iambomi33@konkuk.ac.kr (B.S.); bsj4126@konkuk.ac.kr (S.B.); greenice@konkuk.ac.kr (E.H.); huynhkimhung82@gmail.com (K.-H.H.); hilite2201@naver.com (Y.-H.K.); buzinga5842@konkuk.ac.kr (W.K.); susia45@gmail.com (J.K.); kimde@konkuk.ac.kr (D.-E.K.)

* Correspondence: bjun@konkuk.ac.kr; Tel.: +82-2-450-0521

Abstract: Hydrogen peroxide (H_2O_2) plays important roles in cellular signaling and in industry. Thus, the accurate detection of H_2O_2 is critical for its application. Unfortunately, the direct detection of H_2O_2 by surface-enhanced Raman spectroscopy (SERS) is not possible because of its low Raman cross section. Therefore, the detection of H_2O_2 via the presence of an intermediary such as 3,3,5,5-tetramethylbenzidine (TMB) has recently been developed. In this study, the peroxidase-mimicking activity of gold–silver core–shell-assembled silica nanostructures ($SiO_2@Au@Ag$ alloy NPs) in the presence of TMB was investigated using SERS for detecting H_2O_2 . In the presence of H_2O_2 , the $SiO_2@Au@Ag$ alloy catalyzed the conversion of TMB to oxidized TMB, which was absorbed onto the surface of the $SiO_2@Au@Ag$ alloy. The SERS characteristics of the alloy in the TMB– H_2O_2 mixture were investigated. The evaluation of the SERS band to determine the H_2O_2 level utilized the SERS intensity of oxidized TMB bands. Moreover, the optimal conditions for H_2O_2 detection using $SiO_2@Au@Ag$ alloy included incubating 20 $\mu g/mL$ $SiO_2@Au@Ag$ alloy NPs with 0.8 mM TMB for 15 min and measuring the Raman signal at 400 $\mu g/mL$ $SiO_2@Au@Ag$ alloy NPs.

Keywords: surface-enhanced Raman scattering; gold–silver core–shell; gold–silver core–shell-assembled silica nanostructure; hydrogen peroxide; peroxidase-mimicking catalytic activity; 3,3,5,5-tetramethylbenzidine



Citation: Pham, X.-H.; Seong, B.; Bock, S.; Hahm, E.; Huynh, K.-H.; Kim, Y.-H.; Kim, W.; Kim, J.; Kim, D.-E.; Jun, B.-H. Nonenzymatic Hydrogen Peroxide Detection Using Surface-Enhanced Raman Scattering of Gold–Silver Core–Shell-Assembled Silica Nanostructures. *Nanomaterials* **2021**, *11*, 2748. <https://doi.org/10.3390/nano11102748>

Academic Editor: Angelo Maria Taglietti

Received: 7 September 2021
Accepted: 14 October 2021
Published: 17 October 2021

Publisher's Note: MDPI stays neutral with regard to jurisdictional claims in published maps and institutional affiliations.



Copyright: © 2021 by the authors. Licensee MDPI, Basel, Switzerland. This article is an open access article distributed under the terms and conditions of the Creative Commons Attribution (CC BY) license (<https://creativecommons.org/licenses/by/4.0/>).

1. Introduction

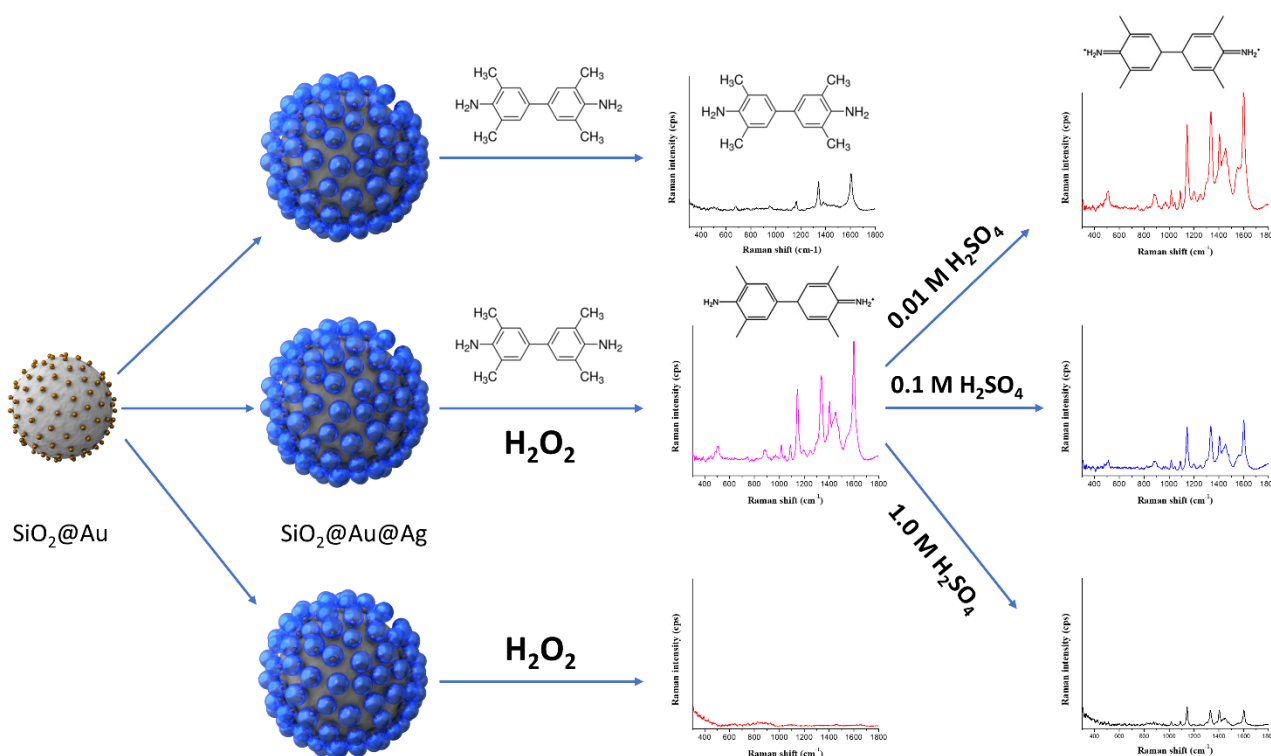
Since the discovery of the peroxidase-mimicking activity of iron (II, III) oxide (Fe_3O_4) on 3,3,5,5-tetramethylbenzidine (TMB), the development of enzyme-free H_2O_2 sensors with peroxidase-like activity has been accelerated [1]. Various nanostructured materials such as noble metal nanostructures [2–8], transition metal oxides [9–11], metal organic frameworks [12–16], and carbon-based nanostructures [17–20] have attracted great interest and have been successfully used to construct enzyme-free H_2O_2 sensors. Unlike native enzymes, nanomaterials possess many advantages, such as ease of preparation, favorable catalytic activity, low cost, and high stability. In particular, the properties of nanomaterials are retained when acting as a nanozyme [1,12,21]. However, the reactive intermediates adsorb to the surface of the nanomaterials and inhibit the catalytic reaction, which limits their applications [22]. In addition, the understanding of the structure/property relation of nanomaterials in H_2O_2 detection is still challenging, in vivo or in vitro [5,14]. Therefore, a sensitive and cost-effective material for detecting H_2O_2 must be developed. Noble metals such as Pt, Pd, Ag, and Au usually show excellent performance for H_2O_2 detection [23]. However, Au nanoparticles (NPs) show catalytic inefficiency in acidic media [12,24], and aggregation at high temperatures reduces their surface-to-volume ratio and limits their

applications [3]. Therefore, the development of stable and high-efficiency nanomaterials as a nanozyme must be further investigated.

Recently, our group developed SiO₂@Au@Ag alloy NPs using a combination of the seed growth method and a SiO₂ template. The distance and uniformity of the Ag shell on SiO₂ NPs was controlled by the Au seed, and the optical properties of the SiO₂@Au@Ag alloy are tunable in the visible to near-infrared region [25–27]. Thus, SiO₂@Au@Ag alloy exhibits a surface-enhanced Raman scattering (SERS) enhancement of 4.2×10^6 with high reproducibility. The designing of an NP structure can be critical for SERS enhancement [28–33]. The SERS enhancement of the SiO₂@Au@Ag alloy NPs is due to the enhancement of the cavity plasmon resonance and the variation of the refractive index of nanomaterials, by lead shifting the operation wavelength and enhancing the local electromagnetic fields of the hotspot region [29,30,33]. Because of their reliability and strength, SiO₂@Au@Ag alloy-based substrates were developed for diagnosing cancers and detecting pesticides, thiram, and glucose [27,34–39]. However, their use in nanozymes and the detection of H₂O₂ using SERS requires further investigation.

The accurate detection of H₂O₂ is critical and has been gaining research attention as H₂O₂ plays important roles both in cellular signaling and in industry [40–42]. Various techniques, including chromatography [43], chemiluminescence [44], fluorescence [45,46], spectrophotometry [47], colorimetry [48], titrimetry [49], and SERS [2,50–52], have been used to detect H₂O₂. Although the electrochemical method is effective for the detection of H₂O₂, the lack of selectivity for interference such as that by oxidative species, because of the similarity of their potential to that of H₂O₂, limits its practical application [22]. Compared with the electrochemical method, SERS exhibits remarkable advantages, such as its indestructibility, fingerprinting, ultrasensitivity, and selectivity [53–57]. Therefore, various NPs, such as Ag and Au nanostructures as SERS substrates, have been fabricated for detecting H₂O₂ [2,50–52]. Unfortunately, the direct detection of H₂O₂ by SERS is not possible because of its low Raman cross section. Therefore, the detection of H₂O₂ via the presence of an intermediary such as TMB has recently been developed. More recently, Ag NPs have been utilized to increase the SERS signals in ELISA via the spontaneous aggregation of Ag NPs with positively charged oxidized TMB (oxTMB). This could be related to the concentration of some biomarkers such as human C-reactive protein or respiratory markers [58,59]. However, the underlying mechanism remains unclear.

In this study, SiO₂@Au@Ag alloy NPs were used as nanozymes and a SERS substrate to develop a method for detecting H₂O₂ via SERS, as outlined in Scheme 1. In the presence of H₂O₂, the SiO₂@Au@Ag alloy NPs catalyze the conversion of TMB to oxTMB, adsorb onto the surface of the SiO₂@Au@Ag alloy NPs, and demonstrate their SERS characteristics. As a result, the SERS band in the presence of H₂O₂ was evaluated by examining the SERS intensity of oxTMB bands on the surface of SiO₂@Au@Ag alloy NPs. This result greatly expands the applicability of this technique for the detection of other biologically active targets based on the adsorption of TMB on SERS substrate.



Scheme 1. Illustration of the peroxidase-mimicking nanozyme activity of gold–silver core–shell-assembled silica alloy suspension ($\text{SiO}_2\text{@Au@Ag}$ alloy nanoparticles) in the presence of 3,3',5,5'-tetramethylbenzidine and H_2O_2 .

2. Materials and Methods

2.1. Preparation of $\text{SiO}_2\text{@Au@Ag}$ Alloy NPs

$\text{SiO}_2\text{@Au@Ag}$ alloy NPs were prepared according to the steps outlined in a previous study [25]. Briefly, $\text{SiO}_2\text{@Au}$ seed was obtained by incubating 10 mL of Au NP suspension and 2 mL of aminated silica NPs overnight. The $\text{SiO}_2\text{@Au@Ag}$ alloy NPs were prepared by reducing 300 μM Ag^+ to Ag on the surface of $\text{SiO}_2\text{@Au}$ in an aqueous medium using ascorbic acid in polyvinylpyrrolidone (PVP). The pellet was obtained by centrifuging the suspension for 15 min at 8500 rpm, washed thoroughly with EtOH, and re-dispersed in absolute EtOH to obtain a 200 $\mu\text{g}/\text{mL}$ $\text{SiO}_2\text{@Au@Ag}$ alloy NP suspension.

2.2. Peroxidase-like Activity of $\text{SiO}_2\text{@Au@Ag}$ Alloy NPs in the TMB and H_2O_2 Mixture in Various Reaction Conditions

To verify the peroxidase-like activity of $\text{SiO}_2\text{@Au@Ag}$ alloy NPs, 10 mM TMB solutions were first prepared in EtOH. Next, 100 μL of TMB solution and 100 μL of $\text{SiO}_2\text{@Au@Ag}$ alloy NPs were added to 100 μL of phosphate-buffered saline (PBS) buffer (pH 7.0) containing freshly prepared H_2O_2 solution. The mixture was incubated for 15 min at 25 $^\circ\text{C}$ and centrifuged at 15,000 rpm for 15 min. The excess reagents were washed thoroughly with PBS containing 0.1% Tween 20 (PBST), and $\text{SiO}_2\text{@Au@Ag@TMB}$ NPs were then re-dispersed in PBST.

2.3. Optimal Peroxidase-like Activity of $\text{SiO}_2\text{@Au@Ag}$ in Various Reaction Conditions

2.3.1. TMB Concentration

Solutions of various TMB concentration were prepared in EtOH. Next, 100 μL of TMB solution, 100 μL of 200 $\mu\text{g}/\text{mL}$ $\text{SiO}_2\text{@Au@Ag}$ alloy NPs, and 100 μL of freshly prepared 2.0 M H_2O_2 solution were added to a pH 7.0 buffer (700 μL) to obtain final concentrations of TMB in the range of 0.1 to 1.0 mM. Each mixture was incubated for 15 min at 25 $^\circ\text{C}$ and centrifuged at 15,000 rpm for 15 min. The $\text{SiO}_2\text{@Au@Ag@TMB}$ NPs were then re-dispersed in PBST (100 μL) to obtain a $\text{SiO}_2\text{@Au@Ag@TMB}$ suspension.

2.3.2. Reaction Time

The effect of reaction time on the SERS signal of SiO₂@Au@Ag alloy NPs was investigated in the mixture containing 8.0 mM TMB solution (100 µL), SiO₂@Au@Ag alloy NPs (0.2 mg/mL, 100 µL), and 2.0 M H₂O₂ solution (100 µL) in a pH 7.0 buffer (700 µL). The mixtures were reacted for 5 to 60 min. The prepared NPs were obtained by centrifuging at 15,000 rpm for 15 min, washed thoroughly, and redispersed in PBST.

2.3.3. Amount of SiO₂@Au@Ag Alloy NPs

To investigate the effect of SiO₂@Au@Ag alloy NP amount on the SERS signal of SiO₂@Au@Ag, 8.0 mM TMB solution (100 µL), 2.0 M H₂O₂ solution (100 µL) and SiO₂@Au@Ag alloy NPs in the range of 10 to 50 µg were added in a pH 7.0 buffer (700 µL). The mixtures were reacted for 15 min at 25 °C, centrifuged for 15 min, washed thoroughly with PBST, and then re-dispersed in PBST (100 µL).

2.3.4. pH Buffer

A 10 mM TMB solution (100 µL), SiO₂@Au@Ag alloy NPs (0.2 mg/mL, 100 µL), and freshly prepared 2.0 M H₂O₂ solution (100 µL) were added to 700 mL of buffers at various pH values ranging from 3.0 to pH 9.0. Next, the mixtures were reacted for 15 min at 25 °C, centrifuged for 15 min, washed thoroughly with PBST, and then re-dispersed in PBST (100 µL).

2.3.5. Concentration of SiO₂@Au@Ag Alloy NPs for Raman Measurement

A 10 mM TMB solution (100 µL), SiO₂@Au@Ag alloy NPs (0.2 mg/mL, 100 µL), and freshly prepared 2.0 M H₂O₂ solution (100 µL) were added to pH 6.0 buffer. Next, the mixtures were reacted for 15 min at 25 °C, centrifuged for 15 min, washed thoroughly with PBST, and then re-dispersed in of PBST. The volume of PBST was adjusted to obtain final concentrations of SiO₂@Au@Ag alloy NPs in the range of 50 to 400 µg/mL for the Raman measurement.

2.3.6. Detection of H₂O₂ using SiO₂@Au@Ag Alloy NPs

A quantity of 20 µg SiO₂@Au@Ag alloy NPs in PBST (100 µL) and 8.0 mM TMB in EtOH (100 µL) were added to pH 6.0 buffer (700 µL). PBS (100 µL) containing different concentrations of H₂O₂ (0.1 to 120 mM) was added to the above-mentioned mixture and allowed to react for 15 min at 25 °C. This mixture was centrifuged for 15 min at 15,000 rpm, washed thoroughly with PBST, and then re-dispersed in PBST to obtain a 400 µg/mL NP suspension for Raman measurement.

2.3.7. Long-Term Stability of SiO₂@Au@Ag Alloy NPs

To investigate the long-term stability of SiO₂@Au@Ag alloy NPs, they were dispersed in EtOH at 200 µg/mL and stored at 4 °C for 60 days. The dispersion of SiO₂@Au@Ag alloy NPs was shaken and diluted to 20 µg/mL. UV-vis spectroscopy was performed at wavelengths of 300 to 800 nm, and the absorbance of the SiO₂@Au@Ag alloy NP suspension at 460 nm was recorded.

2.4. SERS Measurement

The SERS signals were measured at 10 mW for 5 s at randomly selected sites using a micro-Raman system with a 532 nm diode-pumped solid-state laser excitation source and an optical microscope (Olympus BX41, Tokyo, Japan) with a 10× objective lens (0.90 NA, Olympus, Tokyo, Japan). The laser beam spot was ~2.1 µm, and the SERS spectrum in the range of 300–1800 cm⁻¹ was obtained.

3. Results and Discussion

SiO₂@Au@Ag alloy NPs were prepared using a protocol reported by Pham et al. [27,34–39]. The transmission electron microscopy (TEM, JEOL, Akishima, Tokyo) images and UV-vis

extinction spectra (Mecasys, Seoul, Korea) of the SiO₂@Au@Ag alloy NPs are shown in Figure S1. The surface of SiO₂@Au was effectively coated with the Ag shell. Various tiny Au NPs decorated the surfaces of the SiO₂ NPs. The UV–vis extinction spectra of the SiO₂@Au@Ag alloy NPs are consistent with the TEM images (Figure S1b). The as-prepared SiO₂@Au@Ag alloy NP suspension shows the characteristic spectrum in Figure S1 with a broad band from 320 to 700 nm and a maximum peak at ~460 nm. This indicates that Ag shells formed on the SiO₂@Au NP surfaces, created many hot-spot structures, and led a continuous spectrum of resonant multi-modes of the SiO₂@Au@Ag alloy NP suspension [25,27]. These results are consistent with Mie's theory, which states that an increase in particle size leads to a shift of the plasmon absorption band to longer wavelengths [60].

3.1. Peroxidase-Mimicking Nanozyme Activity of SiO₂@Au@Ag Alloy NPs in the TMB–H₂O₂ Mixture

The peroxidase-like activity of the SiO₂@Au@Ag alloy NPs was evaluated through the oxidation of TMB. The oxidation of TMB includes two steps: First, TMB is oxidized to TMB⁺ (oxTMB), and then the clear TMB solution changes to blue in color. However as TMB⁺ is quite unstable, it is oxidized to TMB²⁺ in acidic conditions and exhibits a yellow color [61]. In this study, we investigated the peroxidase-mimicking activity of SiO₂@Au@Ag alloy NPs by mixing 20 µg SiO₂@Au@Ag alloy NPs (i) in 100 µL of H₂O₂ (ii), TMB (iii), and TMB–H₂O₂ mixture (iv) as shown in Figure 1a. The reaction solutions were incubated for 15 min at 25 °C, and the results are shown in Figure 1a. The color of the SiO₂@Au@Ag alloy NP suspension in TMB solution (left column, (iii)) was dark brown and similar to that of SiO₂@Au@Ag (left column, (i)), whereas the SiO₂@Au@Ag alloy NP suspension in H₂O₂ solution (left column, ii) turned grey in color due to its oxidation by H₂O₂ solution. In the presence of TMB and H₂O₂, the color of the SiO₂@Au@Ag alloy NP suspension was light brown (left column, iv). After centrifugation, the supernatant in TMB and H₂O₂ solution in the presence of SiO₂@Au@Ag alloy NPs was transparent and colorless (center column, (ii) and (iii)), indicating that peroxidase-mimicking activity did not occur in the absence of either H₂O₂ or TMB. By contrast, the supernatant in the TMB–H₂O₂ mixture and SiO₂@Au@Ag alloy NPs (center column, (iv)) changed in color from transparent to yellow as shown in Figure 1a(i–iv). The colors of the pellets of SiO₂@Au@Ag alloy NPs after centrifugation and redispersion in PBST are shown in the right-hand column of Figure 1a. Once again, the color of SiO₂@Au@Ag alloy NP suspension (i) was the same as that of SiO₂@Au@Ag alloy NPs with TMB solution (iii), whereas the SiO₂@Au@Ag alloy NP suspensions in H₂O₂ (ii) and a mixture of TMB and H₂O₂ (iv) became light grey and dark grey, respectively. These results imply that SiO₂@Au@Ag alloy NPs possess peroxidase-mimicking activity in the presence of H₂O₂ during the conversion of TMB to oxTMB.

The UV–vis extinction spectra of the SiO₂@Au@Ag alloy NP suspension before and after centrifugation are shown in Figure 1b. The SiO₂@Au@Ag alloy NP suspension without TMB and H₂O₂ showed a broad band from 320 nm to 700 nm with a maximum peak at ~460 nm. The presence of either TMB or H₂O₂ led the UV–vis extinction spectra of the SiO₂@Au@Ag alloy NPs to be slightly red-shifted from ~460 nm to ~500 nm (left column), whereas the suspension of SiO₂@Au@Ag alloy NPs in TMB–H₂O₂ mixture showed a broad and strong peak in the range of 350 nm to 800 nm with clear and multiple peaks at 370 nm and 650 nm [62]. This indicated that TMB was converted to oxTMB in the presence of H₂O₂; this reaction was catalyzed by SiO₂@Au@Ag alloy NPs, as shown in Figure S2. Moreover, the supernatant of the SiO₂@Au@Ag alloy NPs in TMB–H₂O₂ mixture also confirmed the presence of oxTMB when the SiO₂@Au@Ag alloy NPs were removed from the suspension because of the excess oxTMB in the supernatant, which did not adsorb onto the surface of SiO₂@Au@Ag alloy NPs (center column). Therefore, SiO₂@Au@Ag alloy NPs possessed an intrinsic peroxidase-mimicking activity that catalyzed the conversion of TMB to oxTMB, as expected. In addition, the zeta potential values of the SiO₂@Au@Ag alloy NPs in TMB, H₂O₂, and a mixture of TMB and H₂O₂ were also studied, as shown in Figure S3a. SiO₂@Au@Ag alloy NPs showed a zeta potential of -24.5 ± 0.6 mV due to the rich electron

cloud of the Ag layer. The presence of H_2O_2 or TMB in the suspension of $\text{SiO}_2@\text{Au}@Ag$ alloy NPs converted the surface charge to -14.6 ± 0.4 mV or -2.3 ± 0.6 mV, respectively. Thus, the zeta potential of $\text{SiO}_2@\text{Au}@Ag$ alloy NPs increased from -24.5 ± 0.6 mV to -14.6 ± 0.1 mV after adding the TMB– H_2O_2 mixture into the reaction mixture.

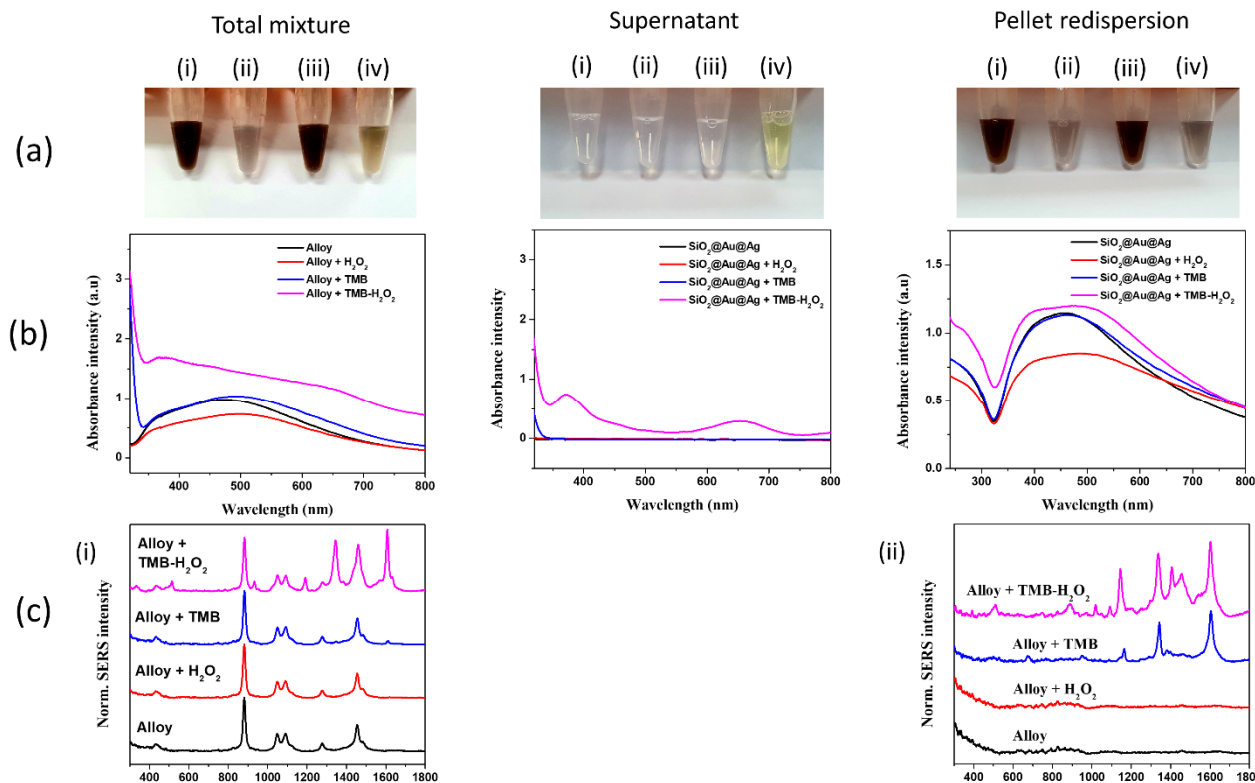


Figure 1. (a) Optical images and (b) ultraviolet–visible (UV–vis) extinction spectra of the peroxidase-mimicking nanozyme activity of the $\text{SiO}_2@\text{Au}@Ag$ alloy NP suspension (left column), pellet redispersion (right column), and supernatant (center column) in (i) the absence of TMB and H_2O_2 and in the presence of (ii) H_2O_2 , (iii) TMB, and (iv) a mixture of TMB and H_2O_2 . (c) Surface-enhanced Raman scattering (SERS) spectra of $\text{SiO}_2@\text{Au}@Ag$ alloy NPs in the TMB– H_2O_2 mixture in (i) EtOH and (ii) PBST at laser excitation of 532 nm. $[\text{H}_2\text{O}_2] = 100$ mM and $[\text{TMB}] = 1$ mM.

In EtOH solution, the Raman spectra of the $\text{SiO}_2@\text{Au}@Ag$ alloy NP suspension in TMB and H_2O_2 are shown in Figure 1c(i). In the $\text{SiO}_2@\text{Au}@Ag$ alloy NP suspension, SERS bands were obtained at 431, 883, 1049, 1093, 1277, and 1455 cm^{-1} , which were assigned to the EtOH solution [27]. New SERS bands of the TMB– H_2O_2 mixture in the presence of $\text{SiO}_2@\text{Au}@Ag$ alloy NPs were also observed at 510, 1191, 1341, 1463, and 1608 cm^{-1} . The bands of the TMB– H_2O_2 mixture at 1341, 1463, and 1608 cm^{-1} were remarkably increased compared to those of the TMB solution. However, the overlap in some EtOH and oxTMB bands and the high background signal of EtOH can hinder analysis and give false results. Therefore, $\text{SiO}_2@\text{Au}@Ag$ alloy NPs must be centrifuged and re-dispersed in PBST, and the Raman spectra must be measured in the PBST solution. Indeed, the SERS bands of EtOH disappeared, and the SERS bands of TMB and oxTMB are clearly observed in Figure 1c(ii). The TMB bands showed typical SERS bands at 1191, 1341, and 1608 cm^{-1} , which correspond to the CN stretching vibration, CH stretching vibration, and CC stretching vibration, respectively [59,62]. The SERS bands of $\text{SiO}_2@\text{Au}@Ag$ alloy NPs in the TMB– H_2O_2 mixture were observed at 1191, 1341, 1468, 1563, and 1608 cm^{-1} . In contrast with the results of a previous study [58,59], oxTMB in our study did not induce the aggregation of Ag NPs but was adsorbed on the surface of $\text{SiO}_2@\text{Au}@Ag$ alloy NPs and showed the characteristic bands of oxTMB as mentioned above. Therefore, these Raman peaks were all used for the measurement of the $\text{SiO}_2@\text{Au}@Ag$ alloy NPs + TMB– H_2O_2 system.

According to the literature [61,63], peroxidase activity was stopped by adding H_2SO_4 to convert oxTMB to TMB^{2+} , which is stable under acidic conditions and possesses an absorbance at 455 nm (Figure S2). The colors of the mixtures of $\text{SiO}_2@\text{Au}@Ag$ alloy NPs and TMB- H_2O_2 after adding H_2SO_4 are shown in Figure 2a (left column). The suspension changed from brown to blue-green at low H^+ concentration (0.01 M H_2SO_4), indicating that oxTMB can partly convert to TMB^{2+} , giving a mix of blue (oxTMB) and yellow (TMB^{2+} in acidic conditions). By contrast, the colors of the mixtures of $\text{SiO}_2@\text{Au}@Ag$ alloy NPs and TMB- H_2O_2 changed from brown to light yellow and yellow, respectively, when 0.1 M and 1.0 M H_2SO_4 were added to the reaction suspension (Figure 2a). This indicates that oxTMB can be completely converted to TMB^{2+} . The results were confirmed by the color of supernatant after centrifugation in Figure 2a (center column).

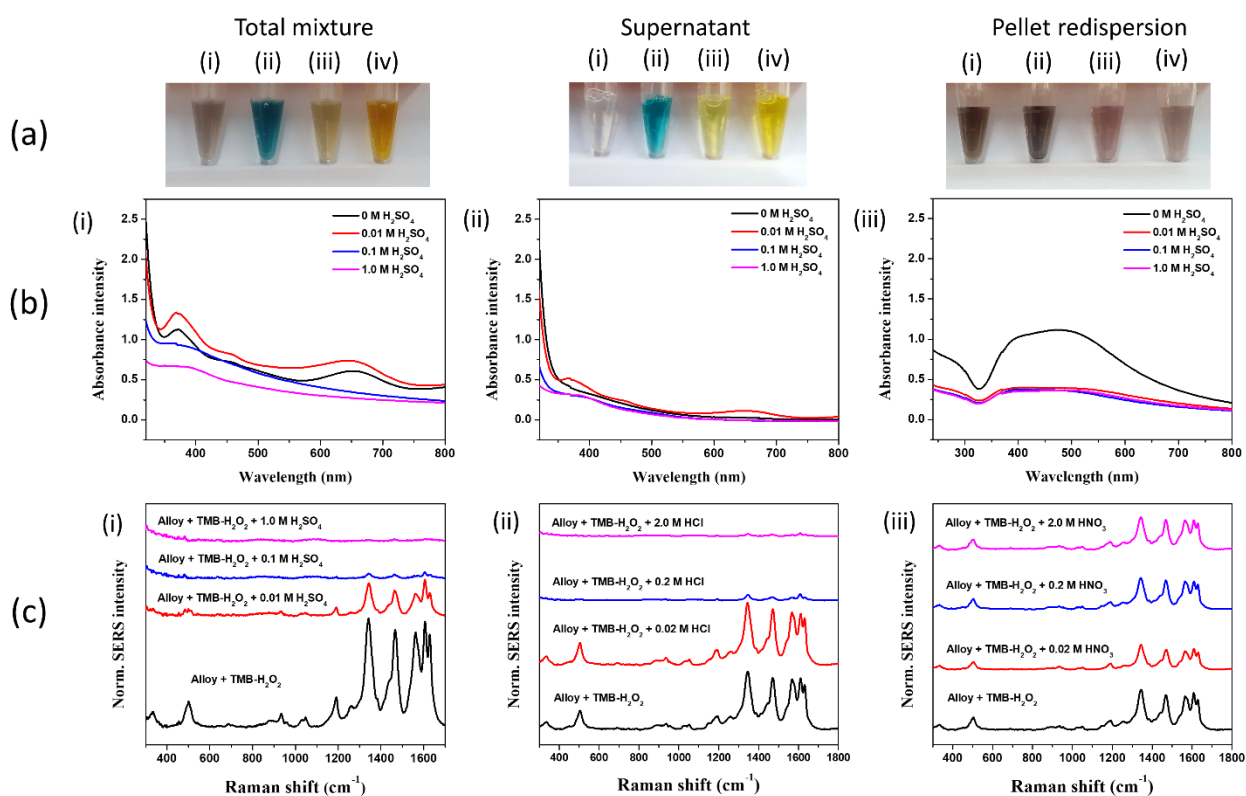


Figure 2. (a) Optical images of $\text{SiO}_2@\text{Au}@Ag$ alloy suspension in the TMB- H_2O_2 mixture after adding (i) 0 M, (ii) 0.01 M, 0.1 M, and 1.0 M H_2SO_4 . (b) UV-vis extinction spectra of (i) $\text{SiO}_2@\text{Au}@Ag$ alloy total suspension, (ii) supernatant, and (iii) pellet redispersion in the mixture of TMB and H_2O_2 at various concentrations of H_2SO_4 . (c) SERS spectra of $\text{SiO}_2@\text{Au}@Ag$ alloy suspension in the mixture of TMB and H_2O_2 after the addition of (i) H_2SO_4 , (ii) HCl, and (iii) HNO_3 . $[\text{H}_2\text{O}_2] = 100$ mM and $[\text{TMB}] = 1$ mM.

The UV-vis extinction spectra of the $\text{SiO}_2@\text{Au}@Ag$ alloy NPs suspensions in TMB- H_2O_2 mixture + H_2SO_4 are consistent with the optical images in Figure 2b. At low H^+ concentrations, the peaks of oxTMB at 370 and 650 nm are clearly observed in Figure 2b(i,ii). These two peaks disappeared after the addition of 0.1 M and 1.0 M H_2SO_4 , indicating the conversion of oxTMB to TMB^{2+} . However, the absorbance intensity of the $\text{SiO}_2@\text{Au}@Ag$ alloy NP pellet collected after centrifugation and redispersion in PBST dramatically decreased with the addition of H_2SO_4 (Figure 2b(iii)).

Furthermore, the SERS signal of $\text{SiO}_2@\text{Au}@Ag$ alloy NP suspension in TMB- H_2O_2 + H_2SO_4 sharply decreased with an increase in H_2SO_4 concentration from 0.01 M to 1.0 M (Figure 2c(i)). The decrease in the SERS signal of oxTMB following the addition of H_2SO_4 was caused by the desorption of oxTMB from the surface of $\text{SiO}_2@\text{Au}@Ag$ alloy NPs and/or low enhancement of the Ag substrate due to the formation of Ag_2SO_4 on the surface of $\text{SiO}_2@\text{Au}@Ag$ alloy NPs. To examine the charge of $\text{SiO}_2@\text{Au}@Ag$ alloy NPs

in TMB–H₂O₂ + H₂SO₄, the zeta potential of SiO₂@Au@Ag alloy NPs in the TMB–H₂O₂ mixture before and after adding H₂SO₄ was measured, as shown in Figure S3b. The zeta potential of SiO₂@Au@Ag alloy NPs increased from -14.6 ± 0.1 mV to -4.4 ± 0.4 mV after the addition of 1.0 M H₂SO₄ to the TMB–H₂O₂ mixture. This result indicates that TMB²⁺ could still be immobilized on the surface of SiO₂@Au@Ag alloy NPs. Therefore, we changed the acidic agent from H₂SO₄ to HCl and HNO₃, while retaining the H⁺ concentration at 2.0 M in the reaction. Similar to that with H₂SO₄, the SERS signal of oxTMB in the SiO₂@Au@Ag alloy NP suspension also decreased slightly with an increase in HCl concentration, possibly because of the formation of AgCl on the surface of SiO₂@Au@Ag alloy NPs (Figure 2c(ii)). By contrast, the SERS signal of oxTMB in SiO₂@Au@Ag alloy NP suspension remained almost the same when 0.2 M and 2.0 M HNO₃ were added. However, the SERS signal of oxTMB slightly decreased when 0.02 M HNO₃ was added to the reaction. This was because the highly water-soluble AgNO₃ was dissolved in the aqueous solution and was not adsorbed on the surface of the SiO₂@Au@Ag alloy NPs. Thus, the decrease in the SERS signal of SiO₂@Au@Ag alloy NPs in TMB–H₂O₂ mixture after adding H₂SO₄ was caused by the formation of Ag₂SO₄, and it decreased the electromagnetic enhancement of the Ag layer on the surface of the SiO₂@Au@Ag alloy NPs. Therefore, we decided not to use acidic conditions to terminate the peroxidase reaction of SiO₂@Au@Ag alloy NPs.

3.2. Effect of Ag⁺ Concentration on the Detection of H₂O₂ by SiO₂@Au@Ag Alloy NPs

According to our previous report, the SERS enhancement of the SiO₂@Au@Ag alloy NPs depends on the gaps between Ag NPs on the surface of SiO₂@Au@Ag alloy NPs, as indicated by adjusting the concentration of AgNO₃ in the solution from 50 to 300 μM [27,38,39]. In Figure 3a, the size of the Au@Ag increased with the concentration of Ag⁺ used.

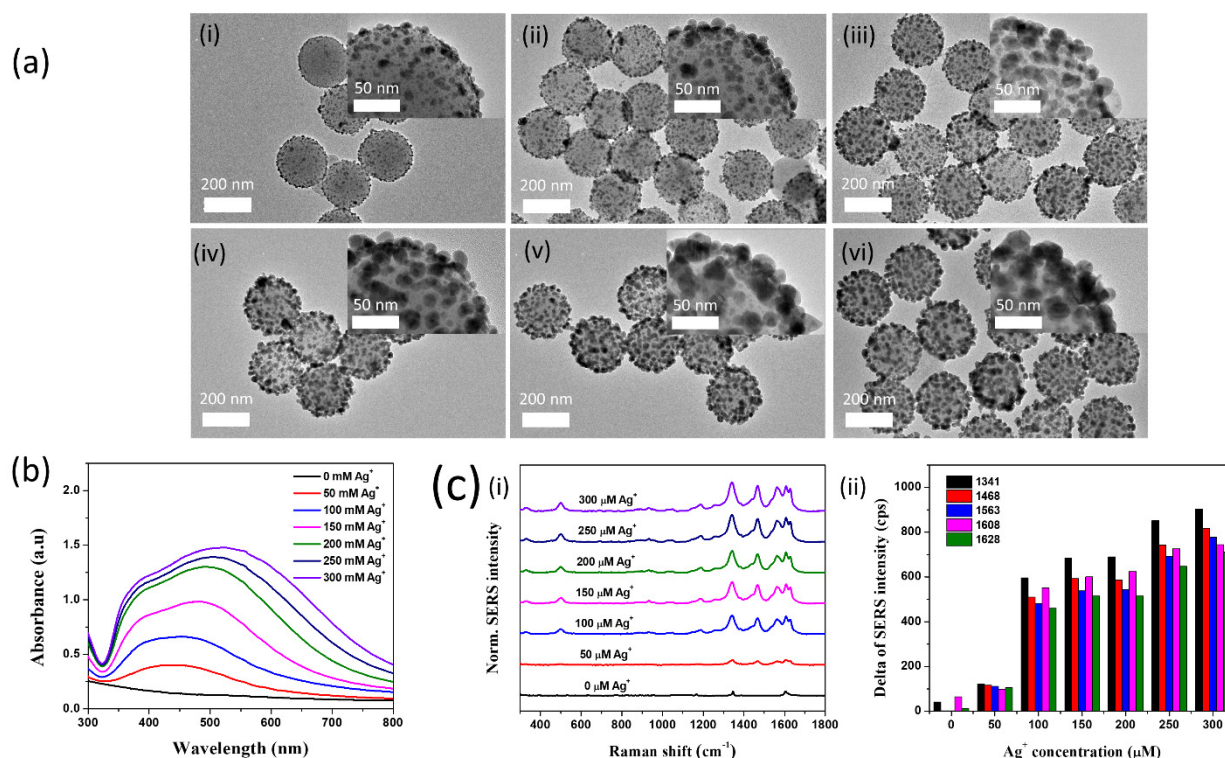


Figure 3. (a) Transmission electron microscopy images and (b) UV–vis extinction spectra of SiO₂@Au@Ag alloy NPs synthesized at various concentration of Ag⁺: (i) 50, (ii) 100, (iii) 150, (iv) 200, (v) 250, and (vi) 300 μM Ag⁺. (c) (i) SERS curves and (ii) SERS signal plot of SiO₂@Au@Ag alloy NPs in TMB–H₂O₂ mixture at various concentration of Ag⁺.

The UV–vis extinction spectra of the SiO₂@Au@Ag alloy NPs shown in Figure 3b are in agreement with the results of TEM images. The maximum UV–vis extinction peak was red-shifted from 450 to 530 nm and broadened from 300 to 800 nm with an increase of Ag⁺

because of the generation of hot-spot structures between two adjacent Au@Ag NPs on the SiO₂@Au@Ag alloy NPs [22,50,64].

The peroxidase-mimicking activities of SiO₂@Au@Ag alloy NPs prepared at various Ag⁺ concentrations toward the TMB–H₂O₂ mixture are shown in Figure 3c. The SERS signal intensities at 1314, 1468, 1563, 1608, and 1628 cm⁻¹ were proportional to the AgNO₃ concentration and highest at 300 μM due to the narrow gaps between Ag NPs on the SiO₂@Au@Ag alloy NP surfaces that created “hot-spots” and strongly enhanced the electromagnetic field surrounding the SiO₂@Au@Ag alloy NPs [33,65]. At higher Ag⁺ concentration, the SiO₂@Au@Ag alloy NPs were aggregated in the TMB–H₂O₂ mixture. Therefore, 300 μM AgNO₃ was the optimal concentration for synthesizing SiO₂@Au@Ag alloy NPs with the highest peroxidase-mimicking activity.

3.3. Optimization of SiO₂@Au@Ag Alloy NPs for Detecting H₂O₂

In the literature, the catalytic activity of nanozymes is also affected by reaction conditions [1,66–70]. The effects of the reaction conditions, including TMB concentration, reaction time, number of SiO₂@Au@Ag alloy NPs, and pH of the buffer, on the peroxidase-mimicking activity of SiO₂@Au@Ag alloy NPs were considered in this study. As mentioned above, the SERS bands of oxTMB at 1191, 1341, 1468, 1563, 1608, and 1628 cm⁻¹ were investigated in the TMB–H₂O₂ mixture. The effects of these conditions on the SERS signal of the SiO₂@Au@Ag alloy NPs in the TMB–H₂O₂ mixture were examined and optimized, as shown in Figure 4.

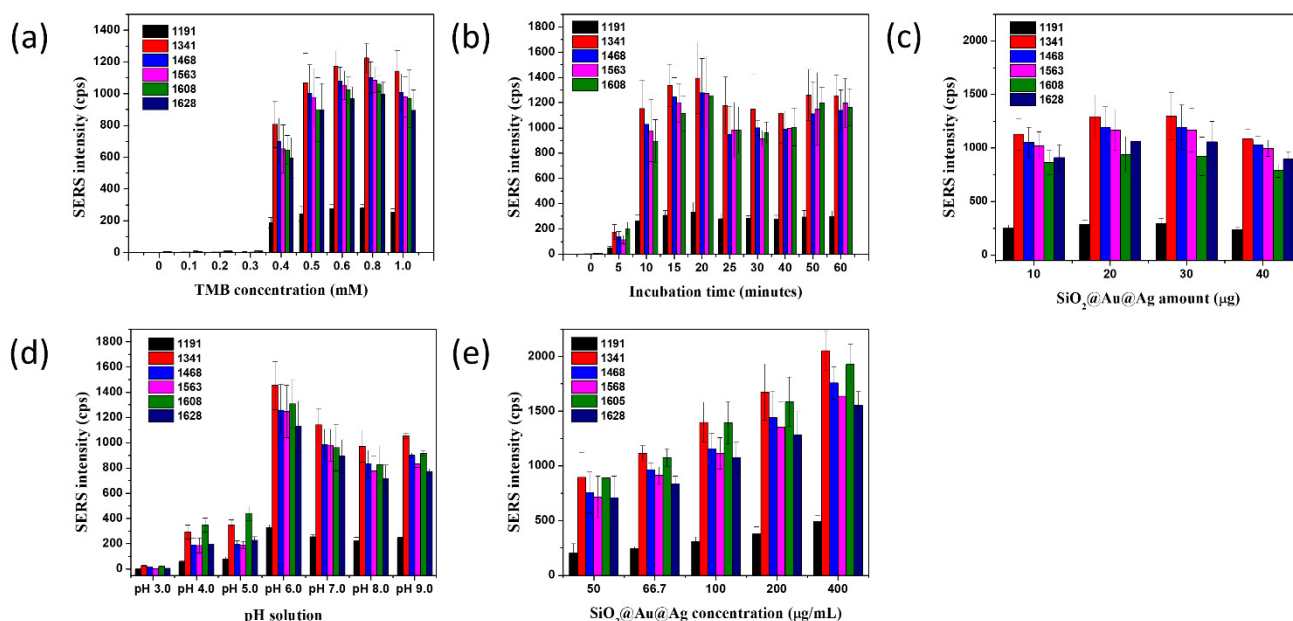


Figure 4. Optimization of H₂O₂ detection using the SiO₂@Au@Ag alloy NPs in the presence of TMB; SERS signal plot at 1191, 1341, 1468, 1563, 1608, and 1628 cm⁻¹ of H₂O₂ at various (a) concentrations of TMB ranging from 0.1 to 1.0 mM, (b) incubation times, (c) amounts of SiO₂@Au@Ag alloy NPs, (d) solution pH, and (e) dilutions of SiO₂@Au@Ag alloy NPs for Raman measurement in PBST.

To establish the effect of TMB concentration on the SERS signal of the SiO₂@Au@Ag alloy NPs in the TMB–H₂O₂ mixture, the concentrations of TMB were investigated in the range of 0 to 1.0 mM (Figure 4a). The SERS signal of SiO₂@Au@Ag alloy NPs was almost insignificant at TMB concentrations lower than 0.4 mM. It increased remarkably when the TMB concentration was higher than 0.4 mM, achieved the highest value at 0.8 mM, but then decreased at higher TMB concentrations because of the poor solubility of TMB in aqueous solution (Figure 4a) [63].

The reaction time or incubation time for detecting H₂O₂ using SiO₂@Au@Ag alloy NPs is also shown in Figure 4b. The SERS signals of oxTMB at 1191, 1341, 1468, 1563,

1608, and 1628 cm^{-1} increased with reaction time and were saturated at 20 min. A gradual decrease in the SERS signal of $\text{SiO}_2\text{@Au@Ag}$ alloy NPs occurred after 20 min, owing to the instability of oxTMB [61].

In addition, the effect of the amount of $\text{SiO}_2\text{@Au@Ag}$ alloy NPs was observed in the range of 10–40 μg , as shown in Figure 4c. The SERS signal is dependent on the Raman reporter density on the nanomaterial surface [26]. Therefore, when a large amount of $\text{SiO}_2\text{@Au@Ag}$ alloy NPs was added, less oxTMB was available on the surface of the $\text{SiO}_2\text{@Au@Ag}$ alloy NPs. The SERS signals at all SERS bands of $\text{SiO}_2\text{@Au@Ag}$ alloy NPs in the TMB– H_2O_2 mixture decreased when 40 μg of $\text{SiO}_2\text{@Au@Ag}$ alloy NPs was used, indicating that the density of oxTMB gradually decreased with an increase in the number of substrates. The SERS signals at all SERS bands of $\text{SiO}_2\text{@Au@Ag}$ alloy NPs increased with a decrease in alloy quantity, as shown in Figure 4c. However, a small amount of $\text{SiO}_2\text{@Au@Ag}$ alloy NPs reduces the peroxidase-mimicking catalytic efficiency of the $\text{SiO}_2\text{@Au@Ag}$ alloy NPs to convert TMB to oxTMB and lower the SERS signal of oxTMB at 10 μg (Figure 4c). Therefore, to ensure that the $\text{SiO}_2\text{@Au@Ag}$ alloy NPs can convert sufficient amounts of TMB to oxTMB in the presence of H_2O_2 , we decided to use 20 μg of $\text{SiO}_2\text{@Au@Ag}$ alloy NPs for further study.

The effect of the pH on the SERS signal of $\text{SiO}_2\text{@Au@Ag}$ alloy NPs in the TMB– H_2O_2 mixture is shown in Figure S4 and Figure 4d. Similar to that of Au, the catalytic activity of $\text{SiO}_2\text{@Au@Ag}$ alloy NPs on H_2O_2 was also pH-dependent. The SERS signal of $\text{SiO}_2\text{@Au@Ag}$ alloy NPs in the TMB– H_2O_2 mixture showed the highest peroxidase-mimicking activity at pH 6.0. At $\text{pH} \leq 4$, the SERS signal of the TMB– H_2O_2 mixture was too weak in all SERS bands. The SERS signal increased in the pH range of 5–6 and then decreased in the pH range of 7–9. In previous reports, the catalytic reaction of TMB– H_2O_2 was much faster in a weakly acidic solution than in neutral or basic solutions. However, in our study, the $\text{SiO}_2\text{@Au@Ag}$ alloy NPs lost 95% of their maximum activity at pH 3.0 and retained ~70% of their maximum activity in the pH range of 7.0–9.0. This is because $\text{SiO}_2\text{@Au@Ag}$ alloy NPs catalyze the generation of $\cdot\text{OH}$ from the decomposition of H_2O_2 with the dissolution of Ag to release Ag^+ under strongly acidic conditions, as shown in the following equation:



The enhancement of the H_2O_2 -reducing ability at high pH led to an increase in the SERS signal of oxTMB. However, under basic conditions, the Ag layer on the surface of $\text{SiO}_2\text{@Au@Ag}$ alloy NPs can be converted to $\text{Ag}(\text{OH})$ or Ag_2O , which lowers the signal enhancement of oxTMB on $\text{SiO}_2\text{@Au@Ag}$ alloy NPs.

For Raman measurement in the liquid phase using a capillary tube, the concentration of the SERS substrate during Raman measurement strongly affects the SERS signal [26,36,38]. Figure 4d shows the effect of the concentration of $\text{SiO}_2\text{@Au@Ag}$ alloy NPs after incubation in the TMB– H_2O_2 mixture. In the absence of H_2O_2 , the SERS signal of the $\text{SiO}_2\text{@Au@Ag}$ alloy NP suspension decreased slightly with increasing concentration of $\text{SiO}_2\text{@Au@Ag}$ alloy NPs for Raman measurements. Moreover, the SERS signals of $\text{SiO}_2\text{@Au@Ag}$ alloy NPs in the TMB– H_2O_2 mixture increased slightly when the concentration of $\text{SiO}_2\text{@Au@Ag}$ alloy NPs decreased sharply. The SERS signal achieved the highest value at 400 $\mu\text{g}/\text{mL}$. Thus, the optimal condition for H_2O_2 detection by $\text{SiO}_2\text{@Au@Ag}$ alloy NPs in TMB– H_2O_2 mixture was achieved at 8 mM TMB for 15 min reaction with 20 μg $\text{SiO}_2\text{@Au@Ag}$ alloy NPs, and Raman measurement was performed at 400 $\mu\text{g}/\text{mL}$ $\text{SiO}_2\text{@Au@Ag}$ alloy NPs.

3.4. Calibration Curve for Detecting H_2O_2

At optimal conditions, the SERS spectra of $\text{SiO}_2\text{@Au@Ag}$ alloy NPs in the presence of TMB were recorded at various concentrations of H_2O_2 . Variation in the SERS signal of $\text{SiO}_2\text{@Au@Ag}$ alloy NPs in the TMB– H_2O_2 mixture was obtained in concentrations of H_2O_2 from 0.1 to 120 mM (Figure 5a). The SERS signals at 1191, 1341, 1468, 1563, 1608, and 1628 cm^{-1} gradually increased when the concentration of H_2O_2 was lower than 20 mM

(Figure 5b). However, they increased remarkably in the range of 40 to 100 mM H_2O_2 . This implies that H_2O_2 efficiently converted TMB to oxTMB and that oxTMB was immobilized on the surface of the $\text{SiO}_2@\text{Au}@Ag$ alloy NPs. The SERS peak reached saturation with an increase in H_2O_2 concentration. This result indicates a complete coverage of oxTMB on the $\text{SiO}_2@\text{Au}@Ag$ alloy NP surfaces. However, the SERS band of oxTMB showed a shift at high H_2O_2 concentration due to the formation of a dimer, a trimer, or the twist of oxTMB on the surface of the $\text{SiO}_2@\text{Au}@Ag$ alloy NPs [71]. Therefore, we concluded that the SERS signal of $\text{SiO}_2@\text{Au}@Ag$ alloy NPs in H_2O_2 solution in the presence of TMB was the result of the catalytic activity involved in the conversion of TMB to oxTMB and the adsorption of oxTMB on the $\text{SiO}_2@\text{Au}@Ag$ alloy NP surfaces.

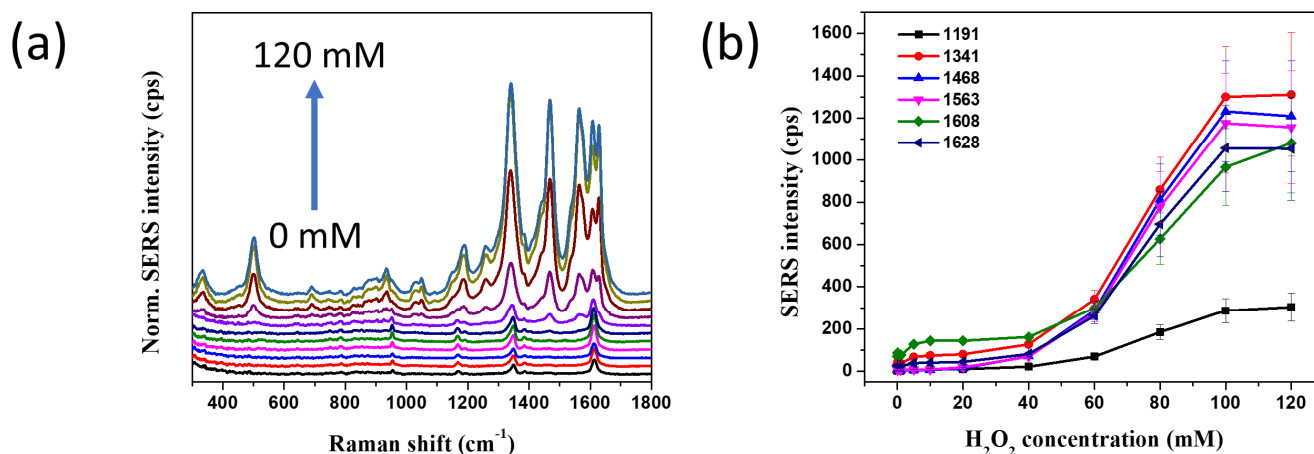


Figure 5. (a) SERS signal curves and (b) SERS plot of $\text{SiO}_2@\text{Au}@Ag$ alloy NPs in TMB– H_2O_2 mixture at various concentrations of hydrogen peroxide from 0 to 120 mM under optimized conditions, which included incubation with 20 μg $\text{SiO}_2@\text{Au}@Ag$ alloy NPs and 0.8 mM TMB for 15 min and Raman measurement at 400 $\mu\text{g}/\text{mL}$ $\text{SiO}_2@\text{Au}@Ag$ alloy NPs.

The calibration of H_2O_2 detection was performed via linear curve fitting in the experimental data points ranging from 40 to 100 mM (Figure S5). A significant linear relationship of $y = 20.04x + 802.17$ was found between the SERS signals and H_2O_2 concentration, where x is the H_2O_2 concentration and y is the SERS signal at 1468 cm^{-1} ($R^2 = 0.98$). The theoretical limit of detection was 33.3 mM, as estimated using the 3 σ blank criterion.

The effect of long-term storage of $\text{SiO}_2@\text{Au}@Ag$ alloy NPs is shown in Figure S6. $\text{SiO}_2@\text{Au}@Ag$ alloy NPs (200 $\mu\text{g}/\text{mL}$) were stored at 4 $^\circ\text{C}$ for 60 days. The UV–vis spectra of the $\text{SiO}_2@\text{Au}@Ag$ alloy NPs were measured at the desired time, and the absorbance at 450 nm was monitored. As shown in Figure S7, the SERS signal was stable for 60 days.

4. Conclusions

We developed a SERS-based H_2O_2 detection method using $\text{SiO}_2@\text{Au}@Ag$ alloy NPs in the presence of TMB. In this work, we demonstrated that TMB was converted to oxTMB by the $\text{SiO}_2@\text{Au}@Ag$ alloy NPs in the presence of H_2O_2 and that oxTMB was adsorbed on the surface of $\text{SiO}_2@\text{Au}@Ag$ alloy NPs. We also provide a calibration curve to evaluate H_2O_2 species in the range of 40 to 100 mM with a limit of detection of 33.3 mM. Moreover, the optimal conditions for H_2O_2 detection using $\text{SiO}_2@\text{Au}@Ag$ alloy NPs include incubating 20 $\mu\text{g}/\text{mL}$ $\text{SiO}_2@\text{Au}@Ag$ alloy NPs with 0.8 mM TMB for 15 min and measuring the Raman signal at 400 $\mu\text{g}/\text{mL}$ of $\text{SiO}_2@\text{Au}@Ag$ alloy NPs. Even though the limit of detection of our structure is not low, it acted as both a nanozyme and a SERS substrate for the adsorption of TMB. This result greatly expands its applicability for the detection of other biologically active targets.

Supplementary Materials: The following are available online at <https://www.mdpi.com/article/10.3390/nano11102748/s1>, Figure S1. (a) Transmission electron microscopy images and (b) ultraviolet-visible extinction spectra of (i) SiO₂@Au (1 mg/mL) and (ii) SiO₂@Au@Ag alloy nanoparticles (NPs) (20 µg/mL) synthesized using 2 mg SiO₂@NH₂ and 300 mM Ag⁺. Figure S2. Schematic illustration of the catalytic mechanism of SiO₂@Au@Ag alloy NPs in the TMB–H₂O₂ mixture. TMB is oxidized to oxTMB by SiO₂@Au@Ag alloy NPs that act as peroxidase in the presence of H₂O₂. Next, oxTMB is converted to TMB²⁺ in the acidic condition. Figure S3. (a) Zeta potential of SiO₂@Au@Ag alloy NPs alone and SiO₂@Au@Ag alloy NPs in the presence of H₂O₂, TMB, and a mixture of TMB and H₂O₂. (b) Zeta potential of SiO₂@Au@Ag alloy NPs in a mixture of TMB and H₂O₂ before and after the addition of H₂SO₄. Figure S4. Surface-enhanced Raman spectroscopy (SERS) signals of SiO₂@Au@Ag alloy NPs in various pH solutions, with pH ranging from 3.0 to 9.0 in the TMB–H₂O₂ mixture. Figure S5. Calibration curves of SERS signal at (a) 1191, (b) 1341, (c) 1468, (d) 1563, (e) 1608, and (f) 1628 cm⁻¹ of SiO₂@Au@Ag alloy NPs in the TMB–H₂O₂ mixture with the concentrations of H₂O₂ ranging from 40 to 100 mM. Figure S6. Long-term storage of 200 µg/mL SiO₂@Au@Ag alloy NPs at 4 °C in ethanol solution.

Author Contributions: Conceptualization, X.-H.P. and B.-H.J.; methodology, W.K., S.B., B.S. and X.-H.P.; investigation, Y.-H.K. and E.H.; formal analysis, K.-H.H. and E.H.; writing—original draft preparation, X.-H.P.; writing—review and editing, J.K. and B.-H.J.; supervisor, D.-E.K. and B.-H.J. All authors have read and agreed to the published version of the manuscript.

Funding: This work was supported by the KU Research Professor Program of Konkuk University. This work was funded by the Ministry of Science and ITC (grant number: NRF-2019R1G1A1006488) and the Ministry of Education (grant number: NRF-2018R1D1A1B07045708).

Data Availability Statement: Data is contained within the article or supplementary material.

Acknowledgments: The authors are grateful for the financial support from the NRF of Korea and Konkuk University.

Conflicts of Interest: The authors declare no conflict of interest.

References

1. Gao, L.; Zhuang, J.; Nie, L.; Zhang, J.; Zhang, Y.; Gu, N.; Wang, T.; Feng, J.; Yang, D.; Perrett, S.; et al. Intrinsic peroxidase-like activity of ferromagnetic nanoparticles. *Nat. Nanotechnol.* **2007**, *2*, 577–583. [[CrossRef](#)] [[PubMed](#)]
2. Chen, Q.; Rao, Y.; Ma, X.; Dong, J.; Qian, W. Raman spectroscopy for hydrogen peroxide scavenging activity assay using gold nanoshell precursor nanocomposites as SERS probes. *Anal. Methods* **2011**, *3*, 274–279. [[CrossRef](#)]
3. Jv, Y.; Li, B.; Cao, R. Positively-charged gold nanoparticles as peroxidase mimic and their application in hydrogen peroxide and glucose detection. *Chem. Commun.* **2010**, *46*, 8017–8019. [[CrossRef](#)]
4. Huang, Z.; Liu, B.; Liu, J. Enhancing the peroxidase-like activity and stability of gold nanoparticles by coating a partial iron phosphate shell. *Nanoscale* **2020**, *12*, 22467–22472. [[CrossRef](#)]
5. Zhuang, Z.; Du, C.; Li, P.; Zhang, Z.; Fang, Z.; Guo, J.; Chen, W. Pt₂₁(C₄O₄SH₅)₂₁ clusters: Atomically precise synthesis and enhanced electrocatalytic activity for hydrogen generation. *Electrochim. Acta* **2021**, *368*, 137608. [[CrossRef](#)]
6. Deng, M.; Xu, S.; Chen, F. Enhanced chemiluminescence of the luminol-hydrogen peroxide system by BSA-stabilized Au nanoclusters as a peroxidase mimic and its application. *Anal. Methods* **2014**, *6*, 3117–3123. [[CrossRef](#)]
7. Nugraha, M.; Pupon, S.; Setyasmara, N. A Study of Palladium-Nickel Catalyst for Direct Synthesis of Hydrogen Peroxide: A DFT Approach. *J. Phys. Sci. Eng.* **2020**, *5*, 10. [[CrossRef](#)]
8. Chang, X.; Batchelor-McAuley, C.; Compton, R.G. Hydrogen peroxide reduction on single platinum nanoparticles. *Chem. Sci.* **2020**, *11*, 4416–4421. [[CrossRef](#)]
9. Hu, Y.; Hojamberdiev, M.; Geng, D. Recent advances in enzyme-free electrochemical hydrogen peroxide sensors based on carbon hybrid nanocomposites. *J. Mater. Chem. C* **2021**, *9*, 6970–6990. [[CrossRef](#)]
10. Zhao, J.; Yang, H.; Wu, W.; Shui, Z.; Dong, J.; Wen, L.; Wang, X.; Yang, M.; Hou, C.; Huo, D. Flexible nickel-cobalt double hydroxides micro-nano arrays for cellular secreted hydrogen peroxide in-situ electrochemical detection. *Anal. Chim. Acta* **2021**, *1143*, 135–143. [[CrossRef](#)]
11. Ma, X.; Tang, K.-I.; Yang, M.; Shi, W.; Zhao, W. A controllable synthesis of hollow pumpkin-like CuO/Cu₂O composites for ultrasensitive non-enzymatic glucose and hydrogen peroxide biosensors. *New J. Chem.* **2020**, *44*, 20411–20418. [[CrossRef](#)]
12. Liu, Y.L.; Zhao, X.J.; Yang, X.X.; Li, Y.F. A nanosized metal-organic framework of Fe-MIL-88NH₂ as a novel peroxidase mimic used for colorimetric detection of glucose. *Analyst* **2013**, *138*, 4526–4531. [[CrossRef](#)] [[PubMed](#)]
13. Hou, C.; Wang, Y.; Ding, Q.; Jiang, L.; Li, M.; Zhu, W.; Pan, D.; Zhu, H.; Liu, M. Facile synthesis of enzyme-embedded magnetic metal-organic frameworks as a reusable mimic multi-enzyme system: Mimetic peroxidase properties and colorimetric sensor. *Nanoscale* **2015**, *7*, 18770–18779. [[CrossRef](#)]

14. Chen, S.; Zhao, P.; Jiang, L.; Zhou, S.; Zheng, J.; Luo, X.; Huo, D.; Hou, C. Cu₂O-mediated assembly of electrodeposition of Au nanoparticles onto 2D metal-organic framework nanosheets for real-time monitoring of hydrogen peroxide released from living cells. *Anal. Bioanal. Chem.* **2021**, *413*, 613–624. [[CrossRef](#)] [[PubMed](#)]
15. Li, B.; Liu, L.-H.; Zhang, X.-F.; Gao, Y.; Deng, Z.-P.; Huo, L.-H.; Gao, S. Novel neuron-network-like Cu–MoO₂/C composite derived from bimetallic organic framework for highly efficient detection of hydrogen peroxide. *Anal. Chim. Acta* **2021**, *1143*, 73–83. [[CrossRef](#)] [[PubMed](#)]
16. Ding, Q.; Wang, J.; Chen, X.; Liu, H.; Li, Q.; Wang, Y.; Yang, S. Quantitative and Sensitive SERS Platform with Analyte Enrichment and Filtration Function. *Nano Lett.* **2020**, *20*, 7304–7312. [[CrossRef](#)] [[PubMed](#)]
17. Maduraiveeran, G.; Jin, W. Carbon nanomaterials: Synthesis, properties and applications in electrochemical sensors and energy conversion systems. *Mater. Sci. Eng. B Solid-State Mater. Adv. Technol.* **2021**, *272*, 115341. [[CrossRef](#)]
18. Speranza, G. Carbon Nanomaterials: Synthesis, Functionalization and Sensing Applications. *Nanomaterials* **2021**, *11*, 967. [[CrossRef](#)]
19. Simsek, M.; Wongkaew, N. Carbon nanomaterial hybrids via laser writing for high-performance non-enzymatic electrochemical sensors: A critical review. *Anal. Bioanal. Chem.* **2021**, *413*, 6079–6099. [[CrossRef](#)]
20. Tao, Y.; Lin, Y.; Huang, Z.; Ren, J.; Qu, X. Incorporating Graphene Oxide and Gold Nanoclusters: A Synergistic Catalyst with Surprisingly High Peroxidase-Like Activity Over a Broad pH Range and its Application for Cancer Cell Detection. *Adv. Mater.* **2013**, *25*, 2594–2599. [[CrossRef](#)]
21. Long, Y.J.; Li, Y.F.; Liu, Y.; Zheng, J.J.; Tang, J.; Huang, C.Z. Visual observation of the mercury-stimulated peroxidase mimetic activity of gold nanoparticles. *Chem. Commun.* **2011**, *47*, 11939–11941. [[CrossRef](#)]
22. Biswas, A.; Eilers, H.; Hidden, F.; Aktas, O.C.; Kiran, C.V.S. Large broadband visible to infrared plasmonic absorption from Ag nanoparticles with a fractal structure embedded in a Teflon AF[®] matrix. *Appl. Phys. Lett.* **2006**, *88*, 013103. [[CrossRef](#)]
23. Trujillo, R.M.; Barraza, D.E.; Zamora, M.L.; Cattani-Scholz, A.; Madrid, R.E. Nanostructures in Hydrogen Peroxide Sensing. *Sensors* **2021**, *21*, 2204. [[CrossRef](#)] [[PubMed](#)]
24. Tian, J.; Liu, S.; Luo, Y.; Sun, X. Fe(iii)-based coordination polymer nanoparticles: Peroxidase-like catalytic activity and their application to hydrogen peroxide and glucose detection. *Catal. Sci. Technol.* **2012**, *2*, 432–436. [[CrossRef](#)]
25. Shim, S.; Pham, X.-H.; Cha, M.G.; Lee, Y.-S.; Jeong, D.H.; Jun, B.-H. Size effect of gold on Ag-coated Au nanoparticle-embedded silica nanospheres. *RSC Adv.* **2016**, *6*, 48644–48650. [[CrossRef](#)]
26. Bong-Hyun, J.; Gunsung, K.; Sinyoung, J.; Suk, N.M.; Xuan-Hung, P.; Homan, K.; Myung-Haing, C.; Jong-Ho, K.; Yoon-Sik, L.; Hong, J.D. Silica Core-based Surface-enhanced Raman Scattering (SERS) Tag: Advances in Multifunctional SERS Nanoprobes for Bioimaging and Targeting of Biomarkers#. *Bull. Korean Chem. Soc.* **2015**, *36*, 963–978. [[CrossRef](#)]
27. Pham, X.-H.; Lee, M.; Shim, S.; Jeong, S.; Kim, H.-M.; Hahm, E.; Lee, S.H.; Lee, Y.-S.; Jeong, D.H.; Jun, B.-H. Highly sensitive and reliable SERS probes based on nanogap control of a Au–Ag alloy on silica nanoparticles. *RSC Adv.* **2017**, *7*, 7015–7021. [[CrossRef](#)]
28. Chou Chau, Y.-F.; Chou Chao, C.-T.; Chiang, H.-P. Ultra-broad bandgap metal-insulator-metal waveguide filter with symmetrical stubs and defects. *Results Phys.* **2020**, *17*, 103116. [[CrossRef](#)]
29. Chou Chau, Y.-F.; Chou Chao, C.-T.; Huang, H.J.; Anwar, U.; Lim, C.M.; Voo, N.Y.; Mahadi, A.H.; Kumara, N.T.R.N.; Chiang, H.-P. Plasmonic perfect absorber based on metal nanorod arrays connected with veins. *Results Phys.* **2019**, *15*, 102567. [[CrossRef](#)]
30. Chou Chau, Y.-F.; Chou Chao, C.-T.; Huang, H.J.; Kooch, M.R.R.; Kumara, N.T.R.N.; Lim, C.M.; Chiang, H.-P. Ultrawide Bandgap and High Sensitivity of a Plasmonic Metal-Insulator-Metal Waveguide Filter with Cavity and Baffles. *Nanomaterials* **2020**, *10*, 2030. [[CrossRef](#)]
31. Chou Chau, Y.-F.; Chou Chao, C.-T.; Rao, J.-Y.; Chiang, H.-P.; Lim, C.M.; Lim, R.C.; Voo, N.Y. Tunable Optical Performances on a Periodic Array of Plasmonic Bowtie Nanoantennas with Hollow Cavities. *Nanoscale Res. Lett.* **2016**, *11*, 411. [[CrossRef](#)]
32. Chou Chau, Y.-F.; Chou Chao, C.-T.; Huang, H.J.; Kooch, M.R.R.; Kumara, N.T.R.N.; Lim, C.M.; Chiang, H.-P. Perfect Dual-Band Absorber Based on Plasmonic Effect with the Cross-Hair/Nanorod Combination. *Nanomaterials* **2020**, *10*, 493. [[CrossRef](#)]
33. Chou Chao, C.-T.; Chou Chau, Y.-F.; Huang, H.J.; Kumara, N.T.R.N.; Kooch, M.R.R.; Lim, C.M.; Chiang, H.-P. Highly Sensitive and Tunable Plasmonic Sensor Based on a Nanoring Resonator with Silver Nanorods. *Nanomaterials* **2020**, *10*, 1399. [[CrossRef](#)]
34. Pham, X.-H.; Hahm, E.; Kang, E.; Ha, Y.N.; Lee, S.H.; Rho, W.-Y.; Lee, Y.-S.; Jeong, D.H.; Jun, B.-H. Gold-silver bimetallic nanoparticles with a Raman labeling chemical assembled on silica nanoparticles as an internal-standard-containing nanoprobe. *J. Alloy. Compd.* **2019**, *779*, 360–366. [[CrossRef](#)]
35. Pham, X.-H.; Hahm, E.; Kang, E.; Son, B.S.; Ha, Y.; Kim, H.-M.; Jeong, D.H.; Jun, B.-H. Control of Silver Coating on Raman Label Incorporated Gold Nanoparticles Assembled Silica Nanoparticles. *Int. J. Mol. Sci.* **2019**, *20*, 1258. [[CrossRef](#)] [[PubMed](#)]
36. Pham, X.-H.; Hahm, E.; Huynh, K.-H.; Son, B.S.; Kim, H.-M.; Jeong, D.H.; Jun, B.-H. 4-Mercaptobenzoic Acid Labeled Gold-Silver-Alloy-Embedded Silica Nanoparticles as an Internal Standard Containing Nanostructures for Sensitive Quantitative Thiram Detection. *Int. J. Mol. Sci.* **2019**, *20*, 4841. [[CrossRef](#)] [[PubMed](#)]
37. Pham, X.-H.; Seong, B.; Hahm, E.; Huynh, K.-H.; Kim, Y.-H.; Kim, J.; Lee, S.H.; Jun, B.-H. Glucose Detection of 4-Mercaptophenylboronic Acid-Immobilized Gold-Silver Core-Shell Assembled Silica Nanostructure by Surface Enhanced Raman Scattering. *Nanomaterials* **2021**, *11*, 948. [[CrossRef](#)] [[PubMed](#)]
38. Pham, X.-H.; Hahm, E.; Kim, T.H.; Kim, H.-M.; Lee, S.H.; Lee, S.C.; Kang, H.; Lee, H.-Y.; Jeong, D.H.; Choi, H.S.; et al. Enzyme-amplified SERS immunoassay with Ag–Au bimetallic SERS hot spots. *Nano Res.* **2020**, *13*, 3338–3346. [[CrossRef](#)]

39. Pham, X.-H.; Hahm, E.; Kim, T.H.; Kim, H.-M.; Lee, S.H.; Lee, Y.-S.; Jeong, D.H.; Jun, B.-H. Enzyme-catalyzed Ag Growth on Au Nanoparticle-assembled Structure for Highly Sensitive Colorimetric Immunoassay. *Sci. Rep.* **2018**, *8*, 6290. [[CrossRef](#)]
40. Yang, H.; Wang, J.; Li, X.; Zhang, L.; Yu, H.; Zhang, L.; Ge, S.; Yu, J.; Zhang, Y. Self-Circulation Oxygen–Hydrogen Peroxide–Oxygen System for Ultrasensitive Cathode Photoelectrochemical Bioassay Using a Stacked Sealed Paper Device. *ACS Appl. Mater. Interfaces* **2021**, *13*, 19793–19802. [[CrossRef](#)]
41. Liu, H.; Weng, L.; Yang, C. A review on nanomaterial-based electrochemical sensors for H₂O₂, H₂S and NO inside cells or released by cells. *Microchim. Acta* **2017**, *184*, 1267–1283. [[CrossRef](#)]
42. Elias, H.; Vayssié, S. Reactive Peroxo Compounds Generated in Situ from Hydrogen Peroxide: Kinetics and Catalytic Application in Oxidation Processes. In *Peroxide Chemistry*; Wiley: Hoboken, NJ, USA, 2000; pp. 128–138. [[CrossRef](#)]
43. Yang, H.; Hu, M.; Li, Z.; Zhao, P.; Xie, L.; Song, X.; Yu, J. Donor/Acceptor-Induced Ratiometric Photoelectrochemical Paper Analytical Device with a Hollow Double-Hydrophilic-Walls Channel for microRNA Quantification. *Anal. Chem.* **2019**, *91*, 14577–14585. [[CrossRef](#)]
44. Wu, Q.; Zhang, C.; Li, F. Preparation of spindle-shape silver core-shell particles. *Mater. Lett.* **2005**, *59*, 3672–3677. [[CrossRef](#)]
45. Jackson, J.B.; Halas, N.J. Silver Nanoshells: Variations in Morphologies and Optical Properties. *J. Phys. Chem. B* **2001**, *105*, 2743–2746. [[CrossRef](#)]
46. Duanghathaipornsuk, S.; Farrell, E.J.; Alba-Rubio, A.C.; Zelenay, P.; Kim, D.-S. Detection Technologies for Reactive Oxygen Species: Fluorescence and Electrochemical Methods and Their Applications. *Biosensors* **2021**, *11*, 30. [[CrossRef](#)]
47. Jiang, Z.-J.; Liu, C.-Y. Seed-Mediated Growth Technique for the Preparation of a Silver Nanoshell on a Silica Sphere. *J. Phys. Chem. B* **2003**, *107*, 12411–12415. [[CrossRef](#)]
48. Ghosal, K.; Sarkar, K. Biomedical Applications of Graphene Nanomaterials and Beyond. *ACS Biomater. Sci. Eng.* **2018**, *4*, 2653–2703. [[CrossRef](#)]
49. Jiang, X.; Wang, H.; Yuan, R.; Chai, Y. Functional Three-Dimensional Porous Conductive Polymer Hydrogels for Sensitive Electrochemiluminescence in Situ Detection of H₂O₂ Released from Live Cells. *Anal. Chem.* **2018**, *90*, 8462–8469. [[CrossRef](#)] [[PubMed](#)]
50. Genov, D.A.; Sarychev, A.K.; Shalaev, V.M. Metal-dielectric Composite Filters With Controlled Spectral Windows of Transparency. *J. Nonlinear Opt. Phys.* **2003**, *12*, 419–440. [[CrossRef](#)]
51. Prodan, E.; Radloff, C.; Halas, N.J.; Nordlander, P. A Hybridization Model for the Plasmon Response of Complex Nanostructures. *Science* **2003**, *302*, 419–422. [[CrossRef](#)] [[PubMed](#)]
52. Yu, Z.; Park, Y.; Chen, L.; Zhao, B.; Jung, Y.M.; Cong, Q. Preparation of a Superhydrophobic and Peroxidase-like Activity Array Chip for H₂O₂ Sensing by Surface-Enhanced Raman Scattering. *ACS Appl. Mater. Interfaces* **2015**, *7*, 23472–23480. [[CrossRef](#)]
53. Harper, M.M.; McKeating, K.S.; Faulds, K. Recent developments and future directions in SERS for bioanalysis. *Phys. Chem. Chem. Phys.* **2013**, *15*, 5312–5328. [[CrossRef](#)]
54. Gong, X.; Bao, Y.; Qiu, C.; Jiang, C. Individual nanostructured materials: Fabrication and surface-enhanced Raman scattering. *Chem. Commun.* **2012**, *48*, 7003–7018. [[CrossRef](#)]
55. Wu, D.-Y.; Li, J.-F.; Ren, B.; Tian, Z.-Q. Electrochemical surface-enhanced Raman spectroscopy of nanostructures. *Chem. Soc. Rev.* **2008**, *37*, 1025–1041. [[CrossRef](#)] [[PubMed](#)]
56. Schlücker, S. Surface-Enhanced Raman Spectroscopy: Concepts and Chemical Applications. *Angew. Chem. Int. Ed.* **2014**, *53*, 4756–4795. [[CrossRef](#)] [[PubMed](#)]
57. Cardinal, M.F.; Vander Ende, E.; Hackler, R.A.; McAnally, M.O.; Stair, P.C.; Schatz, G.C.; Van Duyne, R.P. Expanding applications of SERS through versatile nanomaterials engineering. *Chem. Soc. Rev.* **2017**, *46*, 3886–3903. [[CrossRef](#)] [[PubMed](#)]
58. Zhan, L.; Zhen, S.J.; Wan, X.Y.; Gao, P.F.; Huang, C.Z. A sensitive surface-enhanced Raman scattering enzyme-catalyzed immunoassay of respiratory syncytial virus. *Talanta* **2016**, *148*, 308–312. [[CrossRef](#)]
59. Sloan-Dennison, S.; Laing, S.; Shand, N.C.; Graham, D.; Faulds, K. A novel nanozyme assay utilising the catalytic activity of silver nanoparticles and SERRS. *Analyst* **2017**, *142*, 2484–2490. [[CrossRef](#)]
60. Ortiz-Castillo, J.E.; Gallo-Villanueva, R.C.; Madou, M.J.; Perez-Gonzalez, V.H. Anisotropic gold nanoparticles: A survey of recent synthetic methodologies. *Coord. Chem. Rev.* **2020**, *425*, 213489. [[CrossRef](#)]
61. Josephy, P.D.; Eling, T.; Mason, R.P. The horseradish peroxidase-catalyzed oxidation of 3,5,3',5'-tetramethylbenzidine. Free radical and charge-transfer complex intermediates. *J. Biol. Chem.* **1982**, *257*, 3669–3675. [[CrossRef](#)]
62. Xia, X.; Weng, Y.; Zhang, L.; Tang, R.; Zhang, X. A facile SERS strategy to detect glucose utilizing tandem enzyme activities of Au@Ag nanoparticles. *Spectrochim. Acta A Mol. Biomol. Spectrosc.* **2021**, *259*, 119889. [[CrossRef](#)]
63. Frey, A.; Mecklein, B.; Externest, D.; Schmidt, M.A. A stable and highly sensitive 3,3',5,5'-tetramethylbenzidine-based substrate reagent for enzyme-linked immunosorbent assays. *J. Immunol. Methods* **2000**, *233*, 47–56. [[CrossRef](#)]
64. Bastús, N.G.; Merkoçi, F.; Piella, J.; Puentes, V. Synthesis of Highly Monodisperse Citrate-Stabilized Silver Nanoparticles of up to 200 nm: Kinetic Control and Catalytic Properties. *Chem. Mater.* **2014**, *26*, 2836–2846. [[CrossRef](#)]
65. Chau, Y.-F.C.; Chao, C.-T.C.; Chiang, H.-P.; Lim, C.M.; Voo, N.Y.; Mahadi, A.H. Plasmonic effects in composite metal nanostructures for sensing applications. *J. Nanoparticle Res.* **2018**, *20*, 190. [[CrossRef](#)]
66. Asati, A.; Kaittanis, C.; Santra, S.; Perez, J.M. pH-Tunable Oxidase-Like Activity of Cerium Oxide Nanoparticles Achieving Sensitive Fluorogenic Detection of Cancer Biomarkers at Neutral pH. *Anal. Chem.* **2011**, *83*, 2547–2553. [[CrossRef](#)] [[PubMed](#)]

67. Ge, C.; Fang, G.; Shen, X.; Chong, Y.; Wamer, W.G.; Gao, X.; Chai, Z.; Chen, C.; Yin, J.-J. Facet energy versus enzyme-like activities: The unexpected protection of palladium nanocrystals against oxidative damage. *ACS Nano* **2016**, *10*, 10436–10445. [[CrossRef](#)] [[PubMed](#)]
68. Lin, L.; Song, X.; Chen, Y.; Rong, M.; Zhao, T.; Wang, Y.; Jiang, Y.; Chen, X. Intrinsic peroxidase-like catalytic activity of nitrogen-doped graphene quantum dots and their application in the colorimetric detection of H₂O₂ and glucose. *Anal. Chim. Acta* **2015**, *869*, 89–95. [[CrossRef](#)]
69. Wang, H.; Zheng, L.; Peng, C.; Guo, R.; Shen, M.; Shi, X.; Zhang, G. Computed tomography imaging of cancer cells using acetylated dendrimer-entrapped gold nanoparticles. *Biomaterials* **2011**, *32*, 2979–2988. [[CrossRef](#)]
70. Shah, V.; Shah, S.; Shah, H.; Rispoli, F.J.; McDonnell, K.T.; Workeneh, S.; Karakoti, A.; Kumar, A.; Seal, S. Antibacterial activity of polymer coated cerium oxide nanoparticles. *PLoS ONE* **2012**, *7*, 47827. [[CrossRef](#)]
71. Lin, W.-C.; Jen, H.-C.; Chen, C.-L.; Hwang, D.-F.; Chang, R.; Hwang, J.-S.; Chiang, H.-P. SERS Study of Tetrodotoxin (TTX) by Using Silver Nanoparticle Arrays. *Plasmonics* **2009**, *4*, 187–192. [[CrossRef](#)]